



Evaluating simple proxy measures for estimating depth of the ~1900 nm water absorption feature from hyperspectral data acquired under natural illumination

Richard J. Murphy

Australian Centre for Field Robotics, Department of Aerospace, Mechanical & Mechatronic Engineering, The Rose Street Building J04, The University of Sydney, NSW, Australia



ARTICLE INFO

Article history:

Received 16 December 2014

Received in revised form 22 May 2015

Accepted 31 May 2015

Available online 12 June 2015

Keywords:

Hyperspectral

Water absorption

Atmospheric absorption

Clay minerals

ABSTRACT

Direct measurement of depth of the ~1900 nm feature (F_{1900}) caused by molecular water is not possible from hyperspectral data acquired under natural illumination. Proxy measures for depth were evaluated to estimate the true depth of F_{1900} from such data. Suitable proxy measures were identified using data acquired by a high-resolution spectrometer (under artificial and natural illumination) and by a hyperspectral imaging sensor (under artificial illumination), with different amounts of simulated atmospheric noise. The best performing proxy measures were used to estimate depth from hyperspectral imagery acquired in the field under natural illumination. Proxy measures comprised a ratio of reflectance, continuum-removed depth at a single wavelength and continuum-removed depth integrated over several wavelengths. For high resolution spectra, a ratio of reflectance at 2017 nm and 1967 nm ($\text{Ratio}_{2017/1967}$) and the continuum-removed depth at 1967 nm (CRD_{1967}) were strongly correlated with depth $R^2 = 0.98$ – 0.99 and $R^2 = 0.95$ – 0.96 , respectively. For hyperspectral imagery acquired in the laboratory, $\text{Ratio}_{2017/1967}$ and CRD_{1967} were strongly correlated with depth across all levels of atmospheric noise ($R^2 = 0.94$ – 0.98 and 0.94 – 0.97 , respectively). Proxy measures using integrated depth performed relatively poorly ($R^2 = 0.65$ – 0.86). In independent tests, depth of F_{1900} was consistently overestimated by CRD_{1967} but not by $\text{Ratio}_{2017/1967}$. Validation of field imagery was done by comparing depth predicted by the proxy measures with depth measured from laboratory imagery of collocated samples from the field. $\text{Ratio}_{2017/1967}$ derived from a polynomial fit to the data between 1961 and 2134 nm ($\text{RatioP}_{2017/1967}$) most closely approximated measured depth. $\text{Ratio}_{2017/1967}$, derived from the original data either under or overestimated depth. Measures of continuum-removed depth generated from the original data (CRD_{1967}) and from a polynomial fit to the original data (CRDP_{1967}) overestimated the depth of F_{1900} . This study showed that the depth of F_{1900} can be predicted from data acquired under natural illumination however, the choice of proxy measure can have a significant impact upon quantitative estimates.

© 2015 The Author. Published by Elsevier Inc. This is an open access article under the CC BY-NC-ND license (<http://creativecommons.org/licenses/by-nc-nd/4.0/>).

1. Introduction

There have been many studies which have used hyperspectral imagery to map minerals using their unique spectral curves in the shortwave infrared between 2000–2500 nm (e.g., Ellis & Scott, 2004; Haest et al., 2013; Kruse, 1988; Lagacherie, Baret, Feret, Madeira Netto & Robbez-Masson, 2008; Murphy, Schneider & Monteiro, 2014; Viscarra Rossel & Chen, 2011). Reflectance over spectral regions around 1400 nm and 1900 nm also provides important information relating to mineral composition by detecting the presence of hydroxyl (OH) or bound water which has been adsorbed into the mineral structure or onto the surface of mineral grains (Bishop, Pieters & Edwards, 1994; Clark, 1995). The presence of the feature near 1400 nm, caused by the first overtone of the OH stretch, together with the feature near

1900 nm, caused by combination of the H–O–H bend and the OH stretch indicates the presence of molecular water (Clark, King, Klejwa & Swayze, 1990; Hunt, 1977). The presence of the 1400 nm feature without the 1900 nm feature indicates that only hydroxyl is present. The 1900 nm feature (henceforth termed F_{1900}) is important in the discrimination of smectite-bearing and other hydrated minerals (Bishop et al., 1994; Bishop, Lane, Dyar & Brown, 2008; Chabrilat, Goetz, Krosley & Olsen, 2002; Goetz, Chabrilat & Lu, 2001). In hyperspectral imagery acquired under natural illumination, extracting information on the depth of this feature is relatively straightforward where concentrations of atmospheric water vapour are small, such as on Mars (Bishop & Pieters, 1995; Ehlmann et al., 2009; Mustard et al., 2008; Pelkey et al., 2007). In terrestrial settings however, it has long been recognised that obtaining information from F_{1900} is problematic (e.g., Hunt, 1979). In data acquired under natural illumination, strong absorption by atmospheric water vapour reduces amounts of incident and reflected light so that information

E-mail address: richard.murphy@sydney.edu.au.

over a large proportion of F_{1900} becomes unavailable for most remote sensing applications (Clark, 1999). In the case of F_{1900} , the entire short-wave slope of the feature and the feature minimum (band centre) are obscured by atmospheric noise over the wavelength range of 1810–948 nm. Conventionally, to determine the strength (depth) of an absorption feature, it is necessary to have reflectance values at the band centre (R_b) and the value of the spectral continuum at the same wavelength (R_c). Depth is then determined as $(R_c - R_b)/R_c$ (Clark & Roush, 1984). This measure, often termed continuum-removed depth, scales the depth of the feature to the brightness of the spectrum at that wavelength. Many studies have applied this approach to determine the depth of F_{1900} from reflectance spectra acquired under stable artificial illumination (e.g., Bishop & Pieters, 1995; Cooper & Mustard, 1999; Kariuki, Van Der Meer & Verhoef, 2003; Kariuki, Woldai & Meer, 2004). The wavelength of the band centre of F_{1900} is not constant but can vary with the type of interlayer cation and with moisture content (Bishop et al., 1994). Because neither the wavelength nor the reflectance at the band centre of F_{1900} can be obtained directly from data acquired under natural illumination – proxy measures, derived from data from the long-wave slope of the feature, present the only means by which its depth or relative depth can be estimated. Proxy measures may include ratios or continuum-removed depth at wavelengths including and long-wave of 1948 nm but short-wave of 2100 nm, where reflectance starts to become influenced by the Al-OH absorptions around 2200 nm (Hunt & Salisbury, 1970). The use of wavelengths in this range is, however, not without problems. First, the use of bands long-wave of the band centre will, by definition underestimate the true depth of the F_{1900} because the bands are not at the band centre. Second, F_{1900} is comprised of at least two absorptions – one at ~1910 nm due to bound water attached to cations and a weaker shoulder between ~1950–1970 nm caused by water not attached to cations (Bishop et al., 1994; Cariati, Erre, Micera, Piu & Gessa, 1983; Milliken & Mustard, 2005). As the amount of interlayer water increases (as in the case of smectites) the strength of this shoulder increases. The reflectance on the long-wave slope of F_{1900} is therefore influenced by the type of clay and the amount of adsorbed water, and may not therefore scale linearly with true depth when different types of clay are considered together.

There have been few, if any, studies which have examined explicitly different methods to estimate the true depth of F_{1900} from data acquired under natural illumination. The first objective of this study was therefore to determine if proxy measures were able to predict the depth of F_{1900} using data acquired by a high-resolution, non-imaging field spectrometer from different clay powders and rock samples (Experiment 1). Data were obtained from the same surfaces under natural and artificial illumination. Proxy measures for the depth of F_{1900} were developed using data from the long-wave slope of F_{1900} ; these comprised a ratio of reflectance at different wavelengths and three measures based on continuum-removed depth. Hyperspectral imaging sensors acquire data in a smaller number of broader band-passes and provide numerous spectral measurements of the same sample, enabling variability in measurements to be captured and considered in analyses. Proxy measures were therefore applied to data acquired by an imaging spectrometer under artificial illumination (Experiment 2). Experiment 2 also evaluated the effects of spectral noise on the proxy measures using different amounts of atmospheric noise. The final objective tested the ability of the best performing proxy measures to quantify the depth of F_{1900} on hyperspectral imagery of a vertical rock wall, acquired under natural illumination (Experiment 3). Estimates of depth of F_{1900} from the imagery were validated against measures of actual depth of F_{1900} made in the laboratory from samples acquired from the rock wall.

2. Materials and methods

2.1. Study area and samples

The study area was a vertical rock wall in an open-pit mine in the Pilbara, Western Australia. The geology of the area is characterised by

late Archaean and early Proterozoic rocks including banded iron formation (BIF), and shale horizons. Three thick shale layers, 20 cm→5 m thick and several smaller, less discrete, layers were evident on the rock wall.

Two sets of samples were used in the analyses (Table 1). These comprised commercially-available powdered clay samples and whole rock samples acquired from the rock wall. These were selected because they were very different in their physical characteristics, enabling variability across different materials to be included in the analysis (Table 1). Seven compositionally different powdered clay samples were used which exhibited spectra where the depth of F_{1900} and spectral brightness varied among the samples. To acquire samples from the rock wall, quadrats (0.5 m²) were placed in areas of the shale layers which appeared to be homogenous in colour, brightness and texture (one quadrat per layer, 3 quadrats in total). Between three and 5 representative rock samples were collected from within each quadrat.

The dominant clay mineralogy of the samples was determined by X-ray diffraction (XRD). Samples were ring-milled with an internal standard and micronized. XRD patterns were measured by a Bruker-AXS D8 advance diffractometer with cobalt radiation. Relevant crystal structures extracted for refinement were obtained from the Inorganic Crystal Structure Database (ICSD 2012/1). The crystalline phases were determined on an absolute scale using Rietveld quantitative phase refinement with the Bruker-AXS TOPAS v4.2 software package.

2.2. Data acquisition and preprocessing

2.2.1. High resolution spectroscopy

Spectra (350–2500 nm) were acquired using a field spectrometer (FieldSpec Pro, Analytical Spectral Devices, Boulder, CO; ASD). Three replicate, spatially-independent spectra (henceforth termed high-resolution spectra) were acquired from each clay powder and rock sample under natural and artificial illumination. Clay powders were placed into circular trays, level with the rim of the tray. The spectrometer fibre-optic was fitted with an 8° fore-optic and all spectra were acquired from a height of 15 cm (thus measuring an area on the sample surface of 3.46 cm²). The artificial stable light-source was a 70 W quartz-tungsten-halogen light oriented 30° from nadir, 20 cm away from the sample. Sky conditions were clear, enabling spectra to be acquired under direct illumination. Prior to each sample measurement, a measurement was acquired from a calibration panel (~99% Spectralon®). Each recorded spectrum was an average of 50 individual spectra. First, a calibration and a sample measurement were made under direct sunlight only. Second, without moving the fibre-optic or sample, a calibration and a sample measurement were made under artificial light. To do this, the calibration panel or sample surface was shaded from direct sunlight and some of the scattered (i.e., indirect) light using a large

Table 1

List of samples. Mineral type was identified from the shape of the spectral curve, the wavelength position of diagnostic absorption feature(s) in the spectrum and from XRD analyses.

Sample	Sample label	Sample type	Spectrum	Clay mineralogy (XRD)
1	Kaolinite 1	Clay powder	Kaolinite	Kaolinite
2	Kaolinite 2	Clay powder	Kaolinite	Kaolinite
3	Kaolinite 3	Clay powder	Kaolinite	Kaolinite
4	Kaolinite 4	Clay powder	Kaolinite	Kaolinite
5	Kaolinite 5	Clay powder	Kaolinite	Kaolinite
6	Bentonite	Clay powder	Bentonite	Bentonite
7	Talc	Clay powder	Talc	Talc
8	Shale 1	Whole rock	Kaolinite	Kaolinite
9	Shale 2	Whole rock	Nontronite	Nontronite
10	Shale 3	Whole rock	Kaolinite	Kaolinite
11	Shale 4	Whole rock	Kaolinite	Kaolinite

curved shade. Preliminary tests indicated that the effects of natural scattered light on spectra acquired with artificial light using this method were small. This was because the proportion of scattered light to artificial light was relatively small. After the measurement was taken, the sample was moved so that the process could be repeated for the next replicate measurement.

All spectra were calibrated to absolute reflectance by dividing the sample spectrum by the calibration spectrum and multiplying the result by the panel calibration factor. To remove any small offsets in spectral reflectance between spectra acquired under natural and artificial illumination, the reflectance of former was normalised to the mean reflectance of the latter.

2.2.2. Imaging spectroscopy

Laboratory and field imagery was acquired using a hyperspectral imaging sensor (970–2500 nm; Specim, Finland) which was configured to acquire spectra in 246 bands, each having a resolution of 6.23 nm (full-width-half-maximum; FWHM). The integration time of the sensor was set so that pixels of interest in the imagery were not saturated. All imagery was corrected for dark current.

To acquire laboratory imagery of the powdered clay and from the rock samples, the sensor was mounted on a metal frame, pointing nadir onto a scanning platform below. Samples were placed on the scanning platform at a nominal distance of 730 mm from the sensor and illuminated from opposite directions by two arrays of seven halogen lights each. A measurement from a calibration panel (~99% Spectralon®) comprising 500 frames of data was acquired. Imagery of the samples was acquired with the scanning platform moving. Calibration to absolute reflectance was done on a line-by-line basis by dividing each line in the sample image by the corresponding line in the calibration image and multiplying by the panel calibration factor.

Field imagery of the rock wall was acquired under clear sky conditions, under direct natural illumination. The sensor was mounted on a rotating scanning platform. Calibration panels of variable brightness (~15%, ~30%, ~100% Spectralon® and ~80% Teflon) were placed in the field of view of the sensor. Calibration to reflectance was done using the empirical line method (Roberts, Yamaguchi & Lyon, 1986; Smith & Milton, 1999) using ~15% Spectralon and ~80% Teflon as the dark and bright target respectively. To minimise the effects of noise caused by atmospheric water and CO₂, a 2nd-order polynomial was fitted to data on the long-wave slope of F₁₉₀₀. Tests indicated that a polynomial fitted to data between 1961 and 2134 nm best approximated the generalised shape of the spectral curve over these wavelengths (see Results). Thus, for image data acquired in the field, both the original data and the polynomial fit were used in analyses.

2.3. Determining the relative amounts of spectral noise

To select appropriate wavelength ranges from which to calculate the proxy measures for absorption feature depth it was necessary to determine empirically which wavelengths around F₁₉₀₀ were most affected by noise. Relative amounts of noise at each wavelength were calculated as the peak signal-to-noise ratio (PSNR). PSNR estimated the amount of variation between noise 'free' spectra and spectra with noise. Noise-free spectra are, in this case, either from field or image spectra acquired under artificial light. Spectra with noise are either field spectra acquired under natural light or image spectra acquired under artificial light but with different amounts of added atmospheric noise (see Section 2.4). The PSNR is calculated by:

$$\text{MSE} = \frac{1}{n} \sum_{i=0}^{n-1} (\text{sa} - \text{sn})^2$$

where:

n number of noise-free and noisy spectral pairs
sa noise free spectrum
sn noisy spectrum

$$\text{PSNR} = 10 \cdot \log_{10} \left(\frac{\text{MAXsa}^2}{\text{MSE}} \right)$$

where:

MAXsa maximum possible value for reflectance (i.e., 1)

2.4. Addition of atmospheric noise to imagery

To evaluate the effects of noise on each proxy measure, different amounts of noise were added to hyperspectral imagery acquired in the laboratory. Amount of noise was weighted according to total atmospheric transmission for a standard desert atmosphere generated from the 6S atmospheric model (Verme, Tanré, Deuzé, Herman & Morcette, 1997). Because of this weighting, bands closer to spectral regions where atmospheric water absorbs most had proportionally more noise than bands further away. This approach enabled a direct comparison of the performance of the proxy measures for data acquired, respectively, under artificial light and data with increasing amounts of noise caused by atmospheric absorption. Three different levels of noise were added to give signal-to-noise ratios (SNR) of: 60 dB, 55 dB and 50 dB. Calculation of the PSNR provided an independent estimate of the amount of noise at each wavelength across all spectra.

2.5. Measured depth and proxy measures for depth

2.5.1. Measured depth of F₁₉₀₀

The 'true' or measured depth of F₁₉₀₀ was calculated from high-resolution and image spectra acquired under artificial light. In each case the method was the same. First, the spectral continuum between 1825 and 2154 nm was defined by interpolating between high-points in the spectrum. The continuum was removed by division and the wavelength of maximal absorption (minimal reflectance) identified in the resulting hull-quotients spectrum. The depth of F₁₉₀₀ was then calculated as 1 minus the hull-quotients reflectance at this wavelength (Clark & Roush, 1984).

2.5.2. Proxy measure based on a ratio of reflectance

Many ratios of reflectance could be constructed from wavelengths across the long-wave slope of F₁₉₀₀. For this study, a single 'optimal' ratio was identified from the high-resolution spectra by calculating all possible ratios between 1944 and 2100 nm (156 spectral bands). The ratio which had the largest correlation with measured depth was then selected as the optimal ratio. The shortwave limit of the range was selected because wavelengths shorter than 1944 nm had very small PSNR values (<35 dB) caused by absorption by atmospheric water (the 6S model showed that atmospheric transmission was <10% at these wavelengths). The long-wave limit of the range was selected because it was, on average, approximately coincident with the long-wavelength maximum of F₁₉₀₀. For comparison, separate ratio analyses were constructed from data acquired under natural and artificial illumination, however, only the optimal ratio identified from natural illumination was used as a proxy measure in this study.

The optimal ratio was calculated from high-resolution spectra and from laboratory and field imagery. For field imagery, ratios were calculated from the original (i.e., unsmoothed) data and from the polynomial fit.

2.5.3. Proxy measures based on continuum-removed depth

Continuum-removed depth was calculated for all high-resolution and image spectra in the same way. A hull was fitted to the data over the spectral region 1725–2400 nm, including F₁₉₀₀. High-points

between these wavelengths were identified automatically, ignoring noise spikes where atmospheric water absorption was maximal. The hull was interpolated for all wavelengths over F_{1900} and adjacent spectral regions. Extending the spectral range to 2400 nm ensured that F_{1900} and any absorptions around 2200 nm associated with Al-OH were isolated as separate absorptions. Continuum-removed depth was calculated as 1 minus the hull-quotients value at each wavelength.

Three proxy measures for the depth of F_{1900} were derived from continuum-removed spectra: i) the continuum-removed depth at the wavelength which was maximally correlated with measured depth of F_{1900} ; ii) continuum-removed depth integrated by summing all data between 1944 and 2100 nm (CRD_{SAW}); iii) continuum-removed depth integrated between 1944 nm until the first encounter of a zero value (CRD_{FOZ}) where the spectral curve intersects with the continuum, thus defining the long-wavelength maximum of F_{1900} . For imagery acquired in the field, proxy measures were calculated from the original data and from the polynomial fit.

2.6. Statistical analyses and validation

Relationships between measured depth of F_{1900} and each of the proxy measures were explored using analyses of regression. Separate analyses were done for high-resolution spectra (Experiment 1) and laboratory imagery with different levels of atmospheric noise (Experiment 2). For all laboratory and field imagery, depth was predicted from the proxy measures by applying the coefficients from the respective regression analyses. Depth of F_{1900} predicted from the proxy measures is henceforth termed calibrated depth.

For Experiment 2, data for regression were extracted from imagery of measured depth of F_{1900} and each proxy measure. Pixels ($\times 50$) were randomly-selected from imagery of each clay powder or rock-type ($n = 550$ pixels in total across all samples). Measured depth was then regressed on values for each proxy measure. For validation, a different set of pixels ($n = 550$) were extracted from images of calibrated depth for comparison with measured depth. Differences between

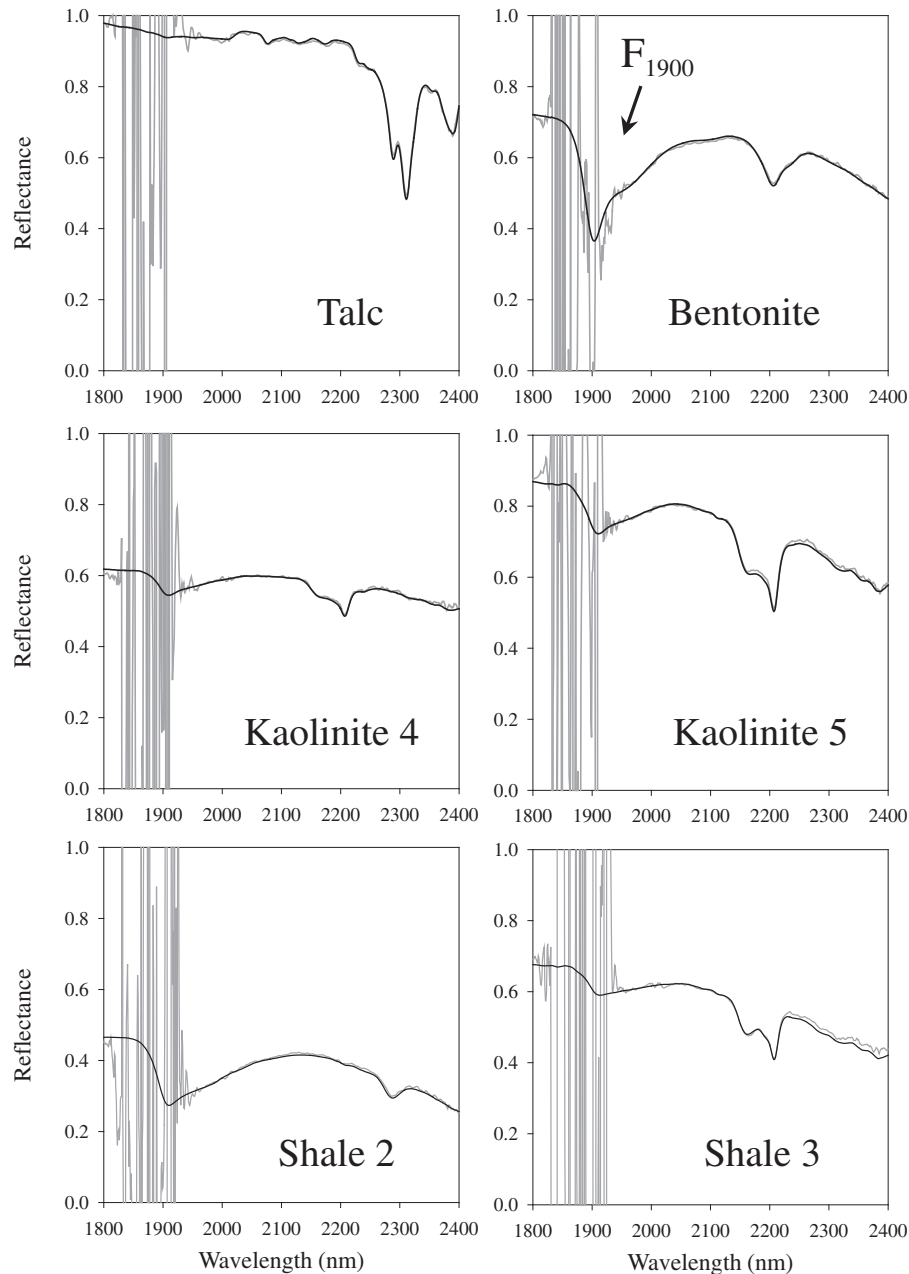


Fig. 1. Example spectra from powdered clays and rock samples showing variability in depth of F_{1900} and spectral brightness (see also Table 1). Spectra were acquired under artificial (black line) and natural illumination (grey line).

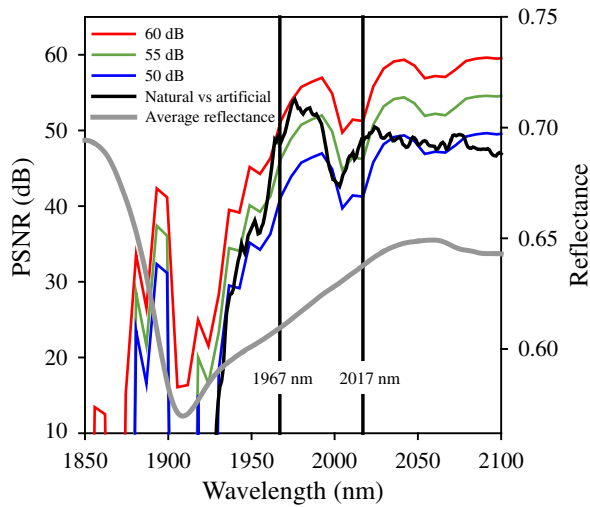


Fig. 2. PSNR as a function of wavelength for high-resolution spectra ('natural vs artificial') and for imagery with each level of atmospheric noise. The average reflectance spectrum of samples is shown (solid grey line). Vertical lines show the wavelengths used in $\text{Ratio}_{2017/1967}$.

measured and calibrated depth were also calculated (measured minus predicted) for all pixels in the image.

For Experiment 3, calibrated depth from field imagery was validated by comparing it to depth measured directly from laboratory imagery of collocated rock samples acquired from the rock wall. Sample locations for Shales 1, 2 & 3 were identified in the field imagery and pixel values

representing calibrated depth were compared with measured depth. Shale 4 was not included in this analysis because it was not present in discrete areas but sparsely scattered on the rock wall, making it difficult to identify in the imagery.

3. Results

3.1. High resolution spectra (Experiment 1)

3.1.1. Spectra

Selected spectra of clay powders and rock samples exhibited marked differences in the depth of F_{1900} (Fig. 1). Among all spectra, talc and bentonite showed, respectively, the smallest and largest depth of F_{1900} . Spectra from other samples showed depths which were intermediate between these (e.g., the two kaolinite samples; Fig. 1). Noise, due to absorption by atmospheric water vapour, masked all information between about 1820–1930 nm in spectra acquired under natural light. The PSNR of spectra acquired under natural light showed a sharp decrease from about 1955 nm to shorter wavelengths, indicating an increase in noise relative to the corresponding spectra acquired under artificial light (Fig. 2).

3.1.2. Ratios

For spectra acquired under natural light, the strongest correlation with measured depth was a ratio of reflectances at 2017 nm and 1967 nm ($\text{Ratio}_{2017/1967}$; $R^2 = 0.98$). These bands were located on the long-wave slope of F_{1900} where amounts of atmospheric noise were relatively small (see Fig. 2). The strongest correlation with depth for spectra acquired under artificial light was a ratio of bands at 2013 and 1964 nm ($R^2 = 0.99$). These wavelengths were very close to those

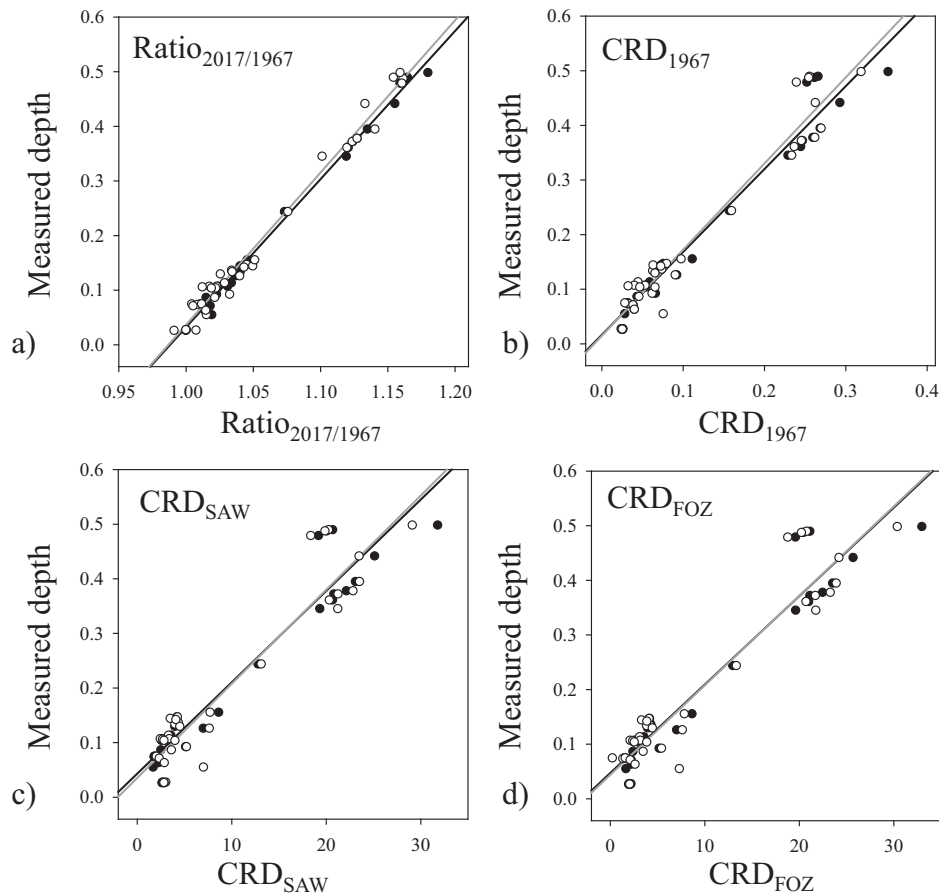


Fig. 3. Measured depth of F_{1900} vs. each of the proxy measures for depth. Data are from high-resolution spectra acquired under artificial (filled circles) and natural light (open circles); a) $\text{Ratio}_{2017/1967}$; b) CRD_{1967} ; c) CRD_{SAW} and d) CRD_{FOZ} . The line of best fit is shown for data acquired under artificial light (black line) and natural light (grey line).

Table 2

Results (R^2 , RMSE, slope, intercept) from regression analyses of measured absorption feature depth on each of the proxy measures for depth determined from data acquired under artificial and natural light (Experiment 1; $n = 36$ paired measurements; $P < 0.0001$ in each case). Data are from high-resolution spectra. The slope and intercept of the regression equations for data acquired under artificial and natural light were not significantly different for all proxy measures.

Method	Artificial				Natural			
	R^2	RMSE	Slope	Intercept	R^2	RMSE	Slope	Intercept
Ratio _{2017/1967}	0.99	0.01	2.71	−2.67	0.98	0.02	2.79	−2.75
CRD ₁₉₆₇	0.96	0.03	1.52	0.02	0.95	0.04	1.58	0.01
Integrated CRD _{SAW}	0.92	0.04	0.02	0.04	0.9	0.05	0.02	0.05
Integrated CRD _{FOZ}	0.92	0.04	0.02	0.05	0.9	0.05	0.02	0.04

found for natural light confirming that a ratio constructed from bands in this part of the spectrum provided a suitable proxy measure for depth of F_{1900} . Because all ratios from spectra acquired under natural light are constrained by the effects of atmospheric noise, Ratio_{2017/1967} was used in all later analyses. Regression of depth on Ratio_{2017/1967} showed a strong linear relationship (Fig. 3; Table 2). Slopes and intercepts of the regressions between measured depth of F_{1900} and Ratio_{2017/1967} derived, respectively, from natural and artificial light were not significantly different (analyses of covariance; ANCOVA).

3.1.3. Continuum-removed depth

For spectra acquired under artificial light, the correlation between measured depth of F_{1900} and continuum-removed depth at individual wavelength was greatest at 1908 nm, a wavelength close to the centre of the F_{1900} (Fig. 4). Correlations between measured and continuum-removed depth were consistently greater for spectra acquired under artificial than under natural light across the wavelength range of F_{1900} (~1850–2100 nm; Fig. 4). For spectra acquired under natural light, the maximal correlation between measured and continuum-removed depth was at 1967 nm (CRD₁₉₆₇; Fig. 4).

Wavelengths shortwave of 1967 nm showed a sharp drop in correlation caused by increased atmospheric noise. Smaller correlations at wavelengths centred on 2012 nm and 2049 nm were associated with increased absorption by atmospheric CO_2 . Regression analysis of measured depth on CRD₁₉₆₇ showed strong linear relationships (Fig. 3; Table 2). Slopes and intercept of the regressions between measured depth of F_{1900} and CRD₁₉₆₇ derived, respectively, from natural and artificial light were not significant (ANCOVA).

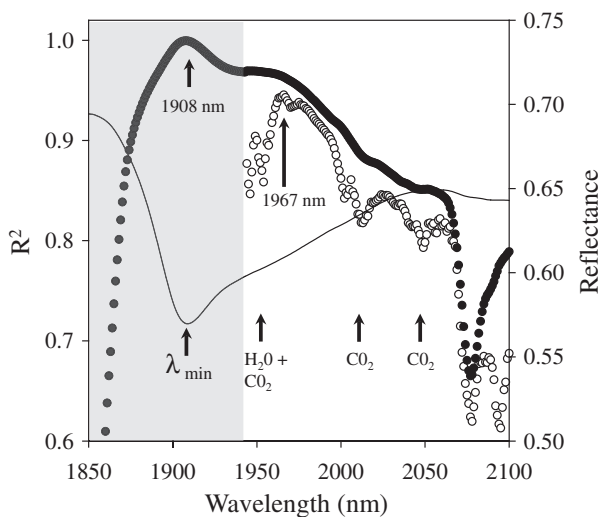


Fig. 4. Correlation (R^2) between measured depth of F_{1900} and continuum-removed depth at individual wavelengths for spectra acquired under artificial light (closed circles) and natural light (open circles). Wavelengths of maximal correlation and decreases in correlation due to atmospheric absorption are indicated. For comparison, the average reflectance spectrum of samples acquired under artificial illumination is shown (black line). The grey area indicates the spectral region where noise obscures all information (data not shown in this area for sake of clarity).

Regression analysis of measured depth F_{1900} and, respectively, CRD_{SAW} and CRD_{FOZ} derived from spectra acquired under artificial and natural light showed strong positive relationships (Fig. 3; Table 2). Compared with other proxy measures, CRD_{SAW} and CRD_{FOZ} showed weaker relationships with measured depth of F_{1900} with a larger RMSE. Analysis of covariance showed that there was no significant difference in the slope and intercept of the regressions between measured depth of F_{1900} and CRD_{SAW} or CRD_{FOZ} derived, respectively, from natural and artificial light.

3.2. Laboratory imagery (Experiment 2)

3.2.1. Atmospheric noise

A laboratory image pixel spectrum with added atmospheric noise is shown with the original spectrum in Fig. 5. Patterns of noise in the spectrum closely approximate those in spectra acquired under natural illumination (cf. Fig. 1). The PSNR from laboratory imagery with different amounts of added atmospheric noise showed similar distributions across wavelengths as did the PSNR measured from field spectra acquired under natural light (Fig. 2). PSNR from imagery, like that measured from field spectra, showed a sharp drop from 1955 nm towards shorter wavelengths, indicating an increase in noise. A decrease in PSNR centred on about 2000 nm was consistent with increased CO_2 absorption. These similarities indicate that image spectra with atmospheric noise are a realistic representation of noise as would be observed from measurements made in the field, enabling proxy measures to be evaluated under different levels of atmospheric noise.

3.2.2. Relationships between measured depth and proxy measures

There was a strong relationship between measured depth and proxy measures for depth of F_{1900} (Fig. 6; Table 3). On average, the strongest

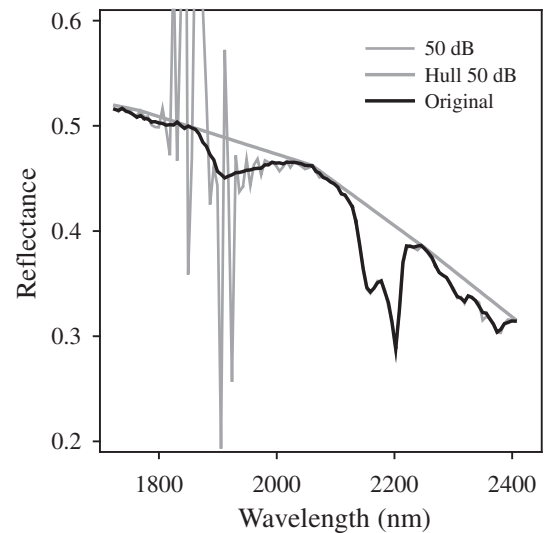


Fig. 5. Image pixel spectrum of Shale 4 before (black line) and after (thin grey line) the addition of atmospheric noise (SNR 50 dB). The continuum (thick grey line) was generated from the spectrum after addition of noise.

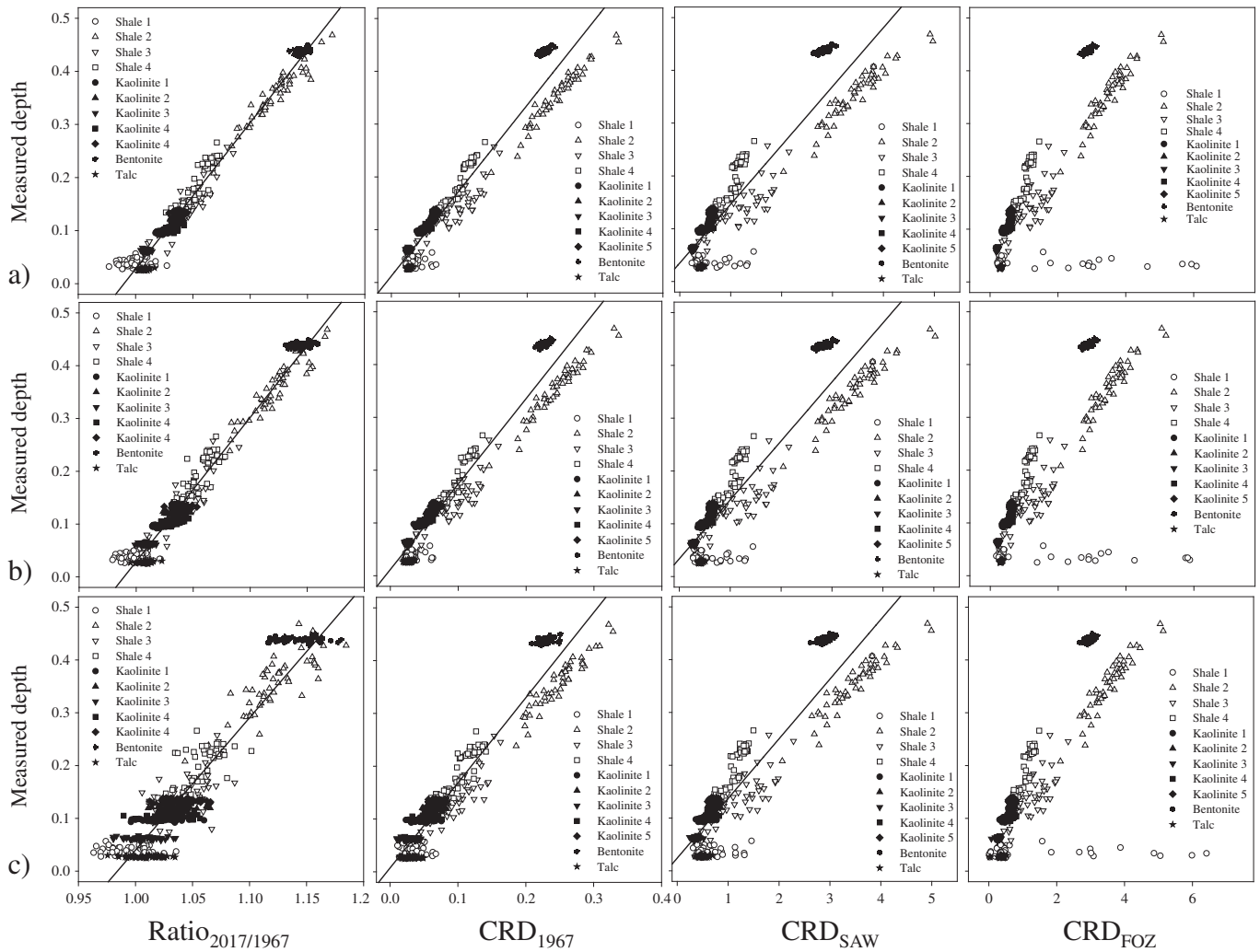


Fig. 6. Measured depth of F_{1900} vs. each of the proxy measures for depth made from hyperspectral imagery: a) data acquired under artificial illumination without added atmospheric noise; b) 60 dB atmospheric noise; c) 50 dB atmospheric noise. Powders (closed symbols), rocks (open symbols).

relationships were found for $\text{Ratio}_{2017/1967}$, followed by CRD_{1967} , CRD_{SAW} and CRD_{FOZ} . The relationship between measured depth and $\text{Ratio}_{2017/1967}$, was linear for all levels of noise, showing no bias around the line of best fit for data from clay powders and rock samples. Relationships between measured depth of F_{1900} and CRD_{1967} showed some samples were distributed with bias around the line of best fit (Bentonite and Shale 2 which were distributed above and below the line, respectively). Despite this bias, correlations remained strong ($R^2 \geq 0.93$) across all levels of noise (Table 3). A similar yet more pronounced bias was

observed in the relationship between measured depth and CRD_{SAW} . No line of best fit could appropriately describe the relationship between measured depth and CRD_{FOZ} because, in addition to the bias, some data (Shale 1) were distributed along a distinctly separate line. Introduction of atmospheric noise to data acquired under artificial light had little or no effect on the strength of the relationship or RMSE of any proxy measure (cf. Fig. 6a, b; Table 3). On the basis of these results, $\text{Ratio}_{2017/1967}$ and CRD_{1967} were selected as the best performing proxy measures. CRD_{SAW} and CRD_{FOZ} were not considered in further analyses.

Table 3

Results (R^2 , RMSE) from regression analyses of measured depth of F_{1900} on selected proxy measures of depth (Experiment 2). Data are from hyperspectral imagery acquired under artificial light and with different amounts of atmospheric noise ($n = 550$). Bold values in the column for R^2 indicate that both slope and intercept coefficients of the regression equation are not significantly different ($P > 0.05$) from those for the original data as determined by analysis of covariance. Note: no appropriate line of best fit could be found for CRD_{FOZ} and therefore no tests for significant differences between regression coefficients were possible.

	$\text{Ratio}_{2017/1967}$		CRD_{1967}		CRD_{SAW}		CRD_{FOZ}	
	R^2	RMSE	R^2	RMSE	R^2	RMSE	R^2	RMSE
Original data	0.98	0.02	0.94	0.03	0.86	0.05	0.65	0.07
60 dB	0.97	0.02	0.94	0.03	0.86	0.05	0.66	0.07
55 dB	0.95	0.03	0.94	0.03	0.86	0.05	0.65	0.07
50 dB	0.9	0.04	0.93	0.03	0.86	0.05	0.66	0.07

3.2.3. Measured vs. predicted depth of F_{1900}

Measured depth was compared to calibrated depth predicted from $\text{Ratio}_{2017/1967}$ and CRD_{1967} . Measured and calibrated depth from $\text{Ratio}_{2017/1967}$ showed a highly linear relationship which followed the 1:1 line (Fig. 7a; Table 4). Spectra from clay powders and rocks were distributed around the 1:1 line without bias. CRD_{1967} , though having a linear relationship with measured depth, showed bias for some samples (Bentonite and Shale 2) around the 1:1 line (Fig. 7; Table 4). This bias was expected given the results from the regression analysis (cf. Fig. 6). The RMSE between measured and calibrated depth indicated that $\text{Ratio}_{2017/1967}$ outperformed CRD_{1967} up until the greatest level of atmospheric noise (50 dB).

Differences between measured depth and calibrated depth from $\text{Ratio}_{2017/1967}$ showed a modal difference of zero, with approximately equal numbers of pixels being distributed about this point (Fig. 8).

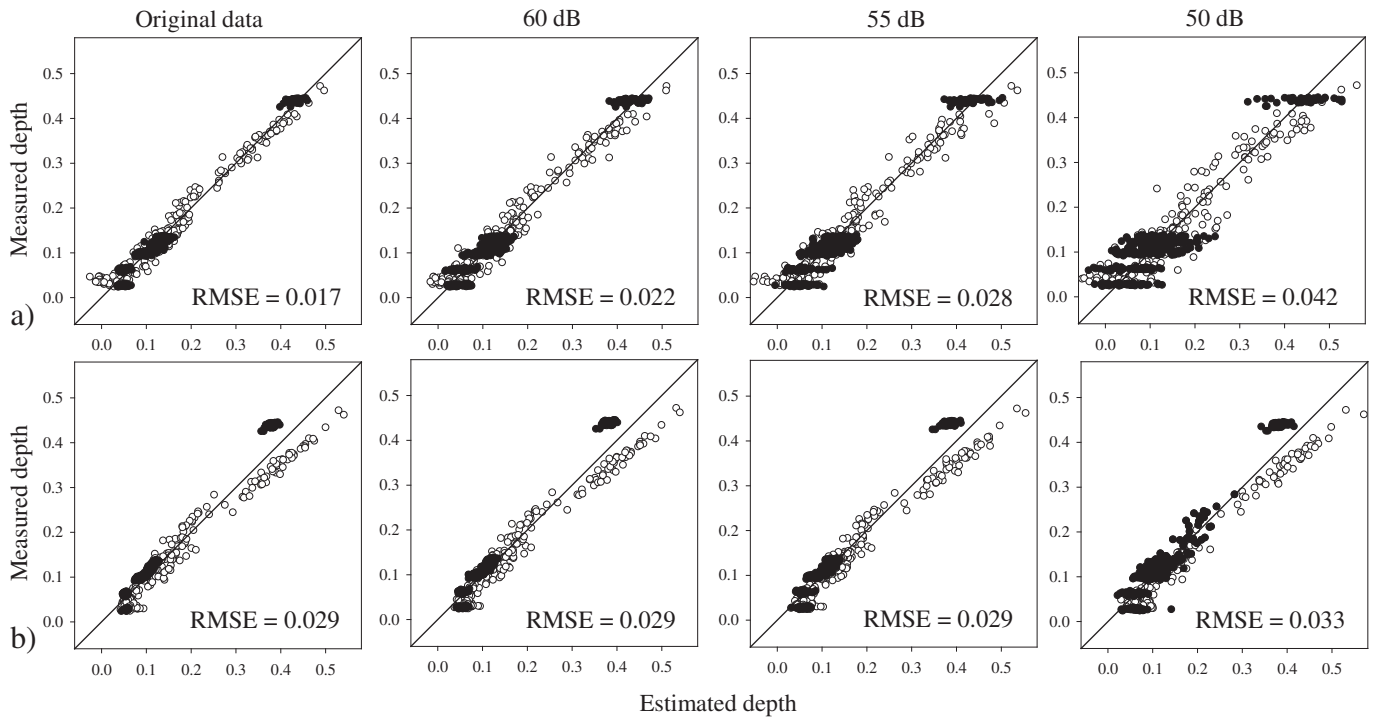


Fig. 7. Measured vs. calibrated depth derived from data before (original data) and after addition of different levels of atmospheric noise (60 dB, 55 dB & 50 dB): a) Ratio_{2017/1967}; b) CRD₁₉₆₇. RMSE is shown at bottom right in each graph (see also Table 4).

Increases in atmospheric noise did not cause the modal value to shift but did cause a progressive flattening of the histograms. Histograms of differences between measured and calibrated depth from CRD₁₉₆₇ had a modal value of about -0.04 , indicating that depth was overestimated (Fig. 8). Some pixels over the rock samples were underestimated by CRD₁₉₆₇. A progressive flattening of the histogram was not evident, as was observed with Ratio_{2017/1967}.

3.2.4. Qualitative analysis of imagery of measured vs. calibrated depth of F_{1900}

The distribution of pixel values in images of calibrated depth from Ratio_{2017/1967} and CRD₁₉₆₇ were similar to that in imagery of measured depth (Fig. 9). Some differences were, however, apparent between measured and calibrated depth. For example, estimates from Ratio_{2017/1967} showed differences with measured depth for Shale 1 (slightly underestimated) and Shale 4 (overestimated over small areas). CRD₁₉₆₇ showed overestimation for Shale 2 and in some areas of Shale 3. These patterns of under and over-estimation were consistent with the location of these samples around the line of best fit (Fig. 6). For example, in Ratio_{2017/1967}, data points for Shale 1 were mainly located above the line of best fit suggesting that depth for Shale 1 would be underestimated. Comparison of calibrated depth derived from imagery with the smallest (60 dB) and largest (50 dB) amounts of atmospheric noise

indicated that, qualitatively, noise had a relatively small impact upon calibrated depth.

3.3. Field imagery (Experiment 3)

3.3.1. Depth of F_{1900}

Image spectra became increasingly noisy towards shorter wavelengths (Fig. 10). The polynomial fitted to the spectrum between 1961 and 2134 nm (solid black line) best described the generalised spectral curve across this range of wavelengths. Images of calibrated depth from proxy measures derived from the original data (Ratio_{2017/1967} and CRD₁₉₆₇) and from the polynomial fit (RatioP_{2017/1967} and CRDP₁₉₆₇) are shown in Fig. 11. Calibrated depth from RatioP_{2017/1967} was less affected by noise than was calibrated depth from Ratio_{2017/1967} (cf. Fig. 11b and c). This improved the quality of the image by reducing high-frequency speckle, particularly over areas of low albedo (cf. Fig. 11b, c at location 'E' in a) and improved the contrast between layers which had discrete differences in calibrated depth (locations 'A' and 'C'). Differences between images of calibrated depth derived from CRD₁₉₆₇ and CRDP₁₉₆₇ were smaller (cf. Fig. 11d, e).

Qualitatively, images of calibrated depth derived from Ratio_{2017/1967} or RatioP_{2017/1967} showed several differences to those derived from CRD₁₉₆₇ or CRDP₁₉₆₇ (cf. Fig. 11 b,c with d,e). First, areas of low albedo were mapped as having a deep absorption by CRD₁₉₆₇ or CRDP₁₉₆₇ but not by Ratio_{2017/1967} or RatioP_{2017/1967} (location 'E' in a). Second, calibrated depth derived from the ratio proxy measure was relatively insensitive to the presence of dead vegetation compared with the calibrated depth derived from the continuum-removed depth proxy measure (location 'B' in a). Third, calibrated depth from the ratio proxy measure was less impacted by variations in illumination caused by topography (locations around 'D' in a). Considered together, these differences suggest that, qualitatively, the proxy measure RatioP_{2017/1967} gave the best estimates of calibrated depth.

Quantitative comparison of calibrated depth derived from field imagery with measured depth of F_{1900} from laboratory imagery of rock samples showed that calibrated depth from RatioP_{2017/1967} was

Table 4

Statistics (RMSE, percent range), comparing measured depth with calibrated depth from Ratio_{2017/1967} and CRD₁₉₆₇ (Experiment 2). Values are rounded up to three decimal places. Percent range is the RMSE expressed as a percentage of the range (0.448) of the measured depth.

Image	Ratio _{2017/1967}		CRD ₁₉₆₇	
	RMSE	Percent range	RMSE	Percent range
Original data	0.017	3.895	0.029	6.374
60 dB	0.022	4.926	0.029	6.447
55 dB	0.028	6.315	0.029	6.564
50 dB	0.042	9.414	0.033	7.290

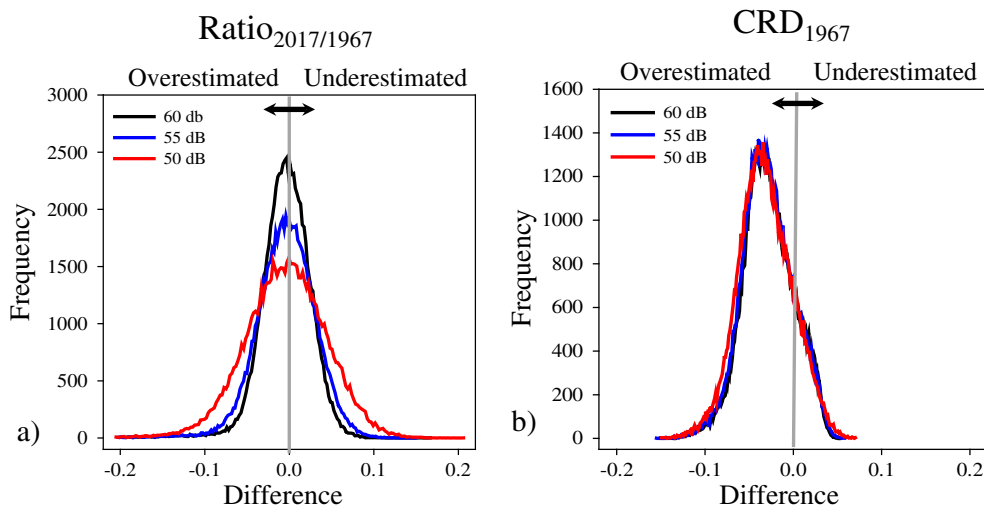


Fig. 8. Histogram of differences between measured and calibrated depth (measured minus calibrated) for all pixels in imagery of rock samples: a) $\text{Ratio}_{2017/1967}$; b) CRD_{1967} . Negative and positive values indicate, respectively, that depth has been over or underestimated by the proxy measure.

consistent with measured depth (Fig. 12). $\text{Ratio}_{2017/1967}$, either under or overestimated depth of F_{1900} (the depth of Shale 1 and Shale 3 was overestimated; depth of Shale 2 was underestimated). With only one exception (CRDP_{1967} ; Shale 3), depth was overestimated by CRD_{1967} and CRDP_{1967} .

4. Discussion

The ability to estimate depth of F_{1900} using proxy measures from data acquired under natural illumination is important for the remote sensing of clays and clay minerals. To date, there has been few, if any,

studies which have assessed how well the depth of F_{1900} could be predicted from proxy measures derived from the long-wave slope of this feature. Using high resolution spectra acquired under natural and artificial illumination, the optimal wavelengths for use in the ratio and continuum-removed depth proxy measures were identified. Reflectance at 1967 nm seems to be closely related to the depth of F_{1900} because it was found to be the denominator in the optimal ratio ($\text{Ratio}_{2017/1967}$) and was also the wavelength where continuum-removed depth was maximally correlated with measured depth (CRD_{1967}). There could be several reasons for this. First, for data acquired under artificial light, the wavelengths with the best correlation

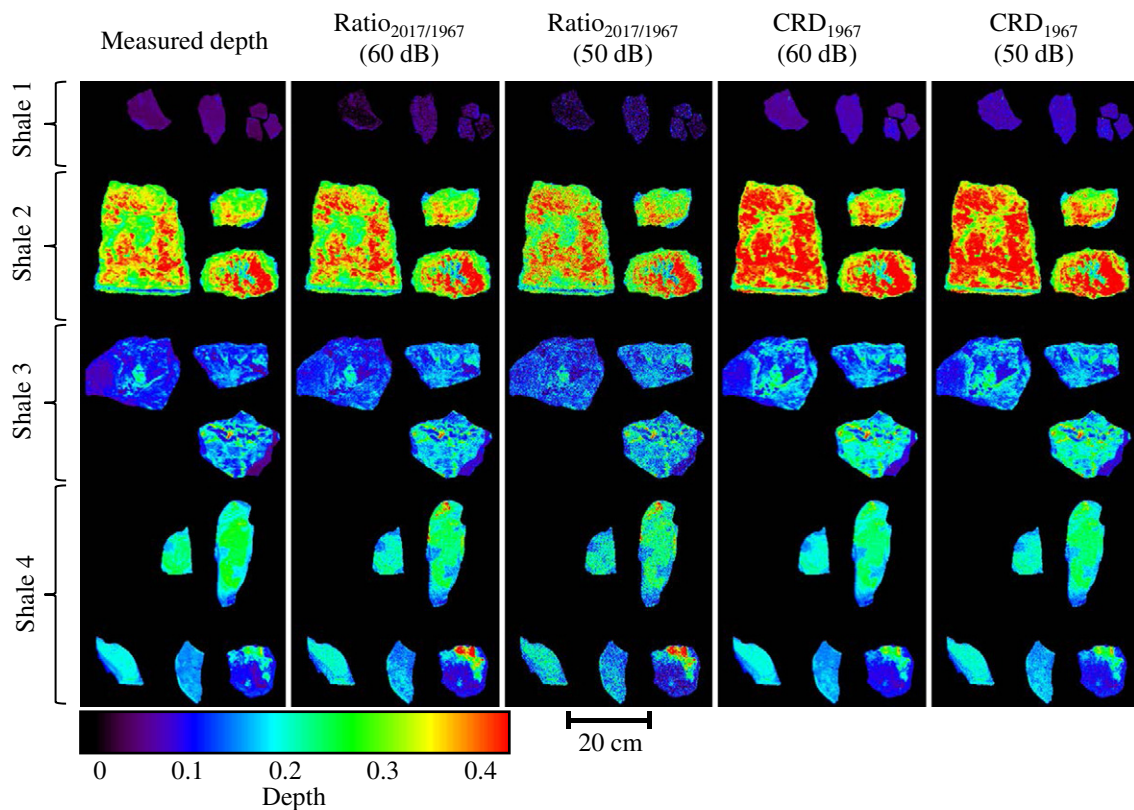


Fig. 9. Imagery of measured and calibrated depth derived from the proxy measures $\text{Ratio}_{2017/1967}$ and CRD_{1967} for data with the smallest and largest amounts of atmospheric noise (60 dB and 50 dB, respectively).

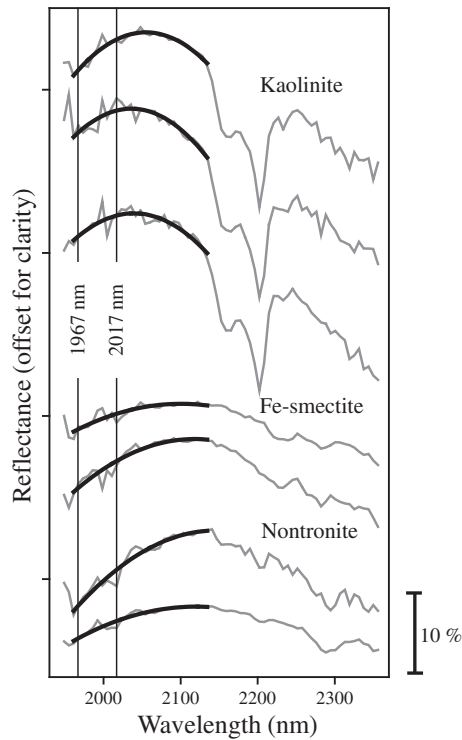


Fig. 10. Single pixel spectra from field imagery. The shape of the spectra and the wavelength position of the absorption features indicate the minerals are kaolinite, Fe-smectite and nontronite. The solid black line is a polynomial fit to the data between 1961 and 2134 nm. Vertical lines indicate the location of the bands used in $\text{Ratio}_{2017/1967}$ or CRD_{1967} .

with depth would be those wavelengths closest to the feature minimum. However, in data acquired under natural light, the wavelength of maximal correlation would be constrained by noise caused by absorption by atmospheric water vapour towards shorter wavelengths and carbon dioxide towards longer wavelengths. Thus, there is a trade-off between proximity to the band centre and avoiding wavelengths affected by atmospheric absorption. Second, several workers have found an absorption shoulder develops at about 1910–1950 nm in minerals which have adsorbed water in their interlayer regions or along grain surfaces, e.g., nontronite or bentonite (Cariati et al., 1983; Milliken & Mustard, 2005). Because both smectite and non-smectite clays are included in this study, the location of 1967 nm in the spectrum relative to the absorption shoulder may represent the location where variation in the proxy measures among samples is minimised with respect to measured depth. It is clear from the analysis of the high-resolution spectra that some proxy measures (i.e., CRD_{SAW} or CRD_{FOZ}) do not work well.

Hyperspectral imagery acquired in the laboratory enabled proxy measures to be evaluated using numerous replicate samples (pixel spectra), allowing spatially independent data to be used to develop regression models and to validate calibrated depth derived from the proxy measures. It also enabled proxy measures to be evaluated using data with different amounts of atmospheric noise. The effects of increasing atmospheric noise were different for the two proxy measures tested on laboratory imagery ($\text{Ratio}_{2017/1967}$ and CRD_{1967}). RMSE between measured and calibrated depth increased with increasing amounts of noise in the case of $\text{Ratio}_{2017/1967}$ but remained constant for CRD_{1967} , albeit at consistently greater values, up until the largest amount of noise (50 dB). Differences between measured depth and calibrated depth indicated that $\text{Ratio}_{2017/1967}$ neither under nor overestimated depth (i.e., mean differences were zero) in data acquired from samples of rock (Shales 1–4). Conversely, CRD_{1967} consistently overestimated the depth of F_{1900} . The reason for this was that samples representing different types of rocks were not evenly distributed around the line of best

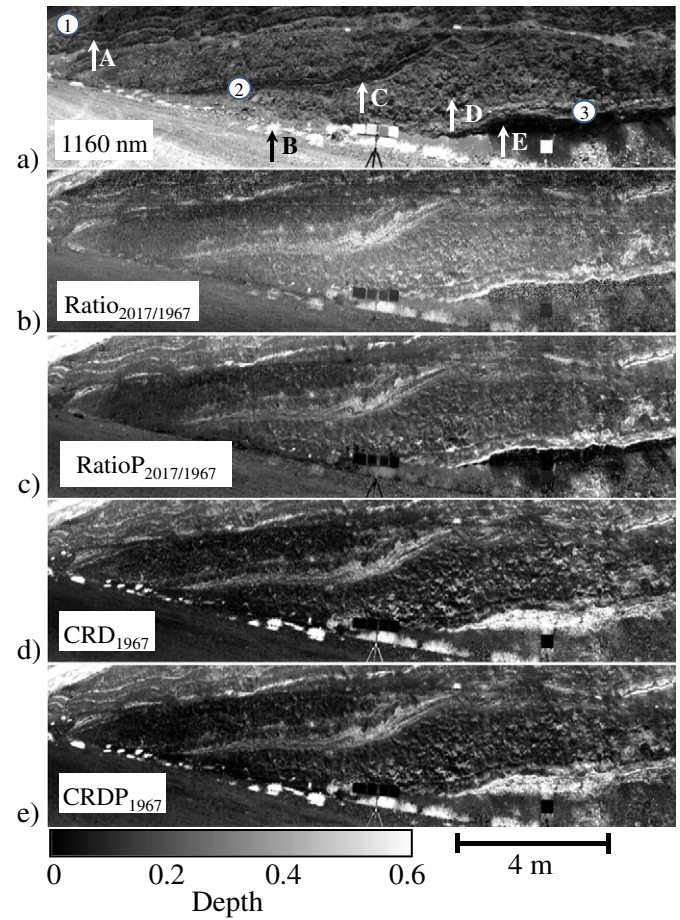


Fig. 11. Calibrated depth of F_{1900} derived from imagery of a vertical rock wall acquired under natural illumination: a) grey-scale image of reflectance at 1160 nm; b) $\text{Ratio}_{2017/1967}$; c) $\text{RatioP}_{2017/1967}$; d) CRD_{1967} ; e) CRDP_{1967} . See text for definition. Plots from where rock samples were taken (solid circles 1–3) and locations in the imagery discussed in the text are indicated in a).

fit describing the relationship between measured depth and CRD_{1967} . This was not the case for $\text{Ratio}_{2017/1967}$.

For hyperspectral imagery acquired in the field, proxy measures were derived from the original data ($\text{Ratio}_{2017/1967}$, CRD_{1967}) and from a polynomial fit to the original data ($\text{RatioP}_{2017/1967}$, CRDP_{1967}). Comparison of calibrated depth from proxy measures derived from field imagery with measured depth from laboratory samples showed that $\text{RatioP}_{2017/1967}$, calculated from a polynomial fit to the original data provided the best match with measured depth. The same proxy measure calculated from the original data ($\text{Ratio}_{2017/1967}$) either under or overestimated measured depth. This suggests that reflectance at either 2017 nm or 1967 nm was affected in some consistent way (i.e., consistently increased or decreased). Closer examination of individual pixel spectra showed that the spectral region centred on 2017 nm showed considerable variability. Many pixel spectra showed a decrease in reflectance, probably caused by incomplete removal of atmospheric carbon dioxide absorption by the reflectance calibration procedure. Increases in reflectance around 2017 nm were also noted in many pixel spectra. A localised increase or decrease in reflectance at or around 2017 nm would translate into an increase or decrease in $\text{Ratio}_{2017/1967}$, leading in turn to an over- or underestimation in the depth of F_{1900} . This effect was removed in the polynomial fit.

Calibrated depth derived from CRD_{1967} or CRDP_{1967} will depend upon how well the continuum can be defined, the exact wavelength intervals used and the overall shape of the spectral curve dictating the architecture of the continuum. In the present study, the continuum was calculated between 1725 nm and 2400 nm. The continuum was not a

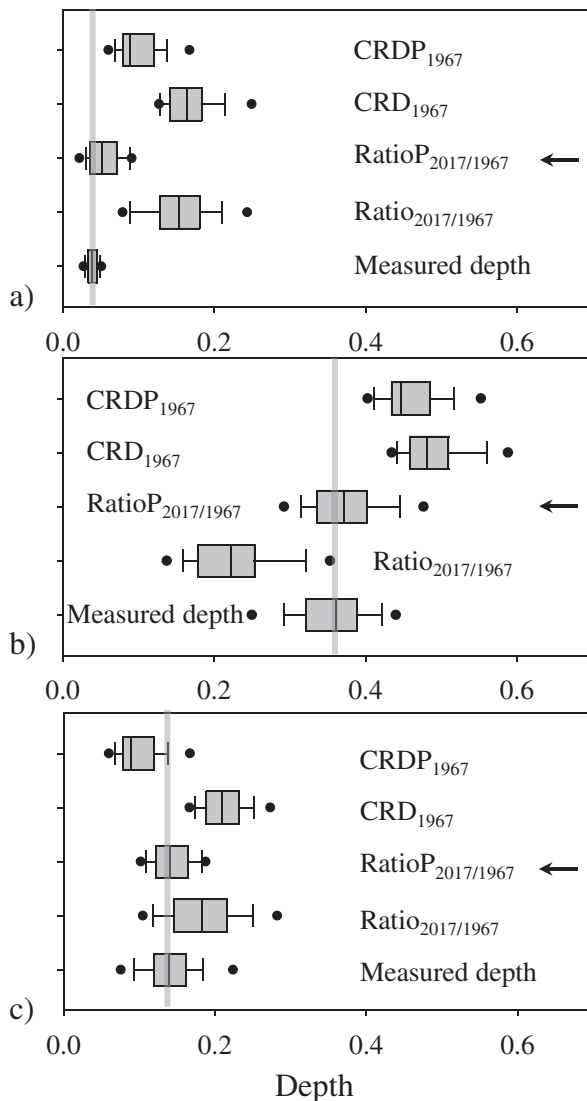


Fig. 12. Calibrated depth from field imagery and measured depth from laboratory imagery of samples taken from the rock wall (locations 1, 2, 3 in Fig. 11a): a) Shale 1; b) Shale 2; c) Shale 3. Median value of the measured depth is shown (vertical lines). In each case, the proxy measure providing the closest approximation of calibrated to measured depth is indicated (black arrows). Graphical elements of the box-plots describe various statistical attributes of the data: box boundaries (25th and 75th percentiles); thin and bold lines bisecting box (median and mean of data, respectively), whiskers (10th and 90th percentiles), filled circles (5th and 95th percentiles of the outliers).

straight line but was interpolated from many straight-line segments between these endpoints. The continuum was defined automatically in this way because the width of F_{1900} , the shape of the spectral curve and the location of clay absorption features between 2000–2400 nm all varied among the different minerals tested. Given this variability, defining a continuum comprised of a single straight line, interpolated from fixed starting and ending wavelengths would not have been appropriate. Nevertheless, it is recognised that automatic definition of the continuum may introduce variability in proxy measures such as CRD_{1967} or $CRDP_{1967}$. This would be especially problematic for data acquired under natural illumination which is often affected by noise, even at wavelengths located outside of the dominant atmospheric absorptions.

Information on the long-wave slope of F_{1900} is commonly ignored in the study of clay minerals using hyperspectral data. This paper has shown that the depth of F_{1900} can be predicted from these data and that calibrated depth is best derived from a ratio of bands rather than continuum-removed depth. Including estimates of the depth of F_{1900} along with other parameters from clay absorption features has the

potential to significantly improve our ability to distinguish between different groups of clay minerals.

5. Conclusions

- i) Several proxy measures, based on ratios of reflectance and continuum-removed depth, were evaluated for estimating depth of ~ 1900 nm (F_{1900}) from hyperspectral data acquired under natural illumination.
- ii) Using high resolution spectra (Experiment 1), the best predictors of the depth of F_{1900} were found to be a ratio of reflectances at 2017 nm and 1967 nm ($Ratio_{2017/1967}$) and the continuum-removed depth at 1967 nm (CRD_{1967}). The two proxy measures based on integrated continuum-removed depth (CRD_{SAW} and CRD_{FOZ}) performed poorly.
- iii) Except for the largest amount of noise, $Ratio_{2017/1967}$ outperformed all other proxy measures in estimating depth of F_{1900} , including CRD_{1967} , from hyperspectral imagery acquired in the laboratory (Experiment 2).
- iv) On average, $Ratio_{2017/1967}$ predicted F_{1900} without bias, neither under or overestimating it. CRD_{1967} , the best performing measure based on continuum-removed depth, consistently overestimated depth of F_{1900} (Experiment 2).
- v) Qualitatively, spatial patterns in depth of F_{1900} measured directly from laboratory imagery were similar to calibrated depth from $Ratio_{2017/1967}$ for data with the smallest (60 dB) and largest (50 dB) amounts of noise (Experiment 2). Conversely, spatial patterns between measured depth and calibrated depth from CRD_{1967} were different.
- vi) Proxy measures derived from field imagery acquired under natural illumination were best calculated from a polynomial fit (Experiment 3). $Ratio_{2017/1967}$ best approximated depth of F_{1900} measured from laboratory imagery of collocated samples.

Acknowledgments

This work has been supported by the Rio Tinto Centre for Mine Automation and the Australian Centre for Field Robotics. The author would like to thank Dr Sven Schneider, Dr Geoff Carter and Tatsumi Uezato for their assistance in the field.

References

- Bishop, J.L., Lane, M.D., Dyar, M.D., & Brown, A.J. (2008). Reflectance and emission spectroscopy study of four groups of phyllosilicates: Smectites, kaolinite-serpentines, chlorites and micas. *Clay Minerals*, 43, 35–54.
- Bishop, J.L., & Pieters, C.M. (1995). Low-temperature and low atmospheric pressure infrared reflectance spectroscopy of Mars soil analog materials. *Journal of Geophysical Research, Planets*, 100, 5369–5379.
- Bishop, J.L., Pieters, C.M., & Edwards, J.O. (1994). Infrared spectroscopic analyses on the nature of water in montmorillonite. *Clays and Clay Minerals*, 42, 702–716.
- Cariati, F., Erre, L., Micera, G., Piu, P., & Gessa, C. (1983). Effects of layer charge on the near-infrared spectra of water molecules in smectites and vermiculites. *Clays and Clay Minerals*, 31, 447–449.
- Chabrilat, S., Goetz, A.F.H., Krosley, L., & Olsen, H.W. (2002). Use of hyperspectral images in the identification and mapping of expansive clay soils and the role of spatial resolution. *Remote Sensing of Environment*, 82, 431–445.
- Clark, R.N. (1995). Reflectance spectra. In T.J. Ahrens (Ed.), *AGU reference shelf 3, rock physics and phase relations, a handbook of physical constants. American Geophysical Union*. (pp. 178–188).
- Clark, R.N. (1999). Spectroscopy of rocks, and minerals and principles of spectroscopy. In A.N. Rencz, & R.A. Ryerson (Eds.), *Remote sensing for the earth sciences, manual of remote sensing* (pp. 3–58). New York, NY: John Wiley & Sons.
- Clark, R.N., King, T.V.V., Klejwa, M., & Swayze, G.A. (1990). High spectral resolution reflectance spectroscopy of minerals. *Journal of Geophysical Research*, 95, 12653–12680.
- Clark, R.N., & Roush, T.L. (1984). Reflectance spectroscopy: Quantitative analysis techniques for remote sensing applications. *Journal of Geophysical Research*, 89, 6329–6340.
- Cooper, C.D., & Mustard, J.F. (1999). Effects of very fine particle size on reflectance spectra of smectite and palagonitic soil. *Icarus*, 142, 557–570.
- Ehlmann, B.L., Mustard, J.F., Swayze, G.A., Clark, R.N., Bishop, J.L., Poulet, F., et al. (2009). Identification of hydrated silicate minerals on Mars using MRO-CRISM: Geologic

- context near Nili Fossae and implications for aqueous alteration. *Journal of Geophysical Research, Planets*, 114.
- Ellis, R.J., & Scott, P.W. (2004). Evaluation of hyperspectral remote sensing as a means of environmental monitoring in the St. Austell China clay (kaolin) region, Cornwall, UK. *Remote Sensing of Environment*, 93, 118–130.
- Goetz, A.F.H., Chabrilat, S., & Lu, Z. (2001). Field reflectance spectrometry for detection of swelling clays at construction sites. *Field Analytical Chemistry and Technology*, 5, 143–155.
- Haest, M., Cudahy, T., Rodger, A., Laukamp, C., Martens, E., & Caccetta, M. (2013). Unmixing the effects of vegetation in airborne hyperspectral mineral maps over the Rocklea Dome iron-rich palaeochannel system (Western Australia). *Remote Sensing of Environment*, 129, 17–31.
- Hunt, G.R. (1977). Spectral signatures of particulate minerals in the visible and near infrared. *Geophysics*, 42, 501–513.
- Hunt, G.R. (1979). Near-infrared (1.3–2.4) μm spectra of alteration minerals—Potential for use in remote sensing. *Geophysics*, 44, 1974–1986.
- Hunt, G.R., & Salisbury, J.W. (1970). Visible and near-infrared spectra of minerals and rocks: I silicate minerals. *Modern Geology*, 1, 283–300.
- Kariuki, P.C., Van Der Meer, F., & Verhoef, P.N.W. (2003). Cation exchange capacity (CEC) determination from spectroscopy. *International Journal of Remote Sensing*, 24, 161–167.
- Kariuki, P.C., Woldai, T., & Meer, F.V.D. (2004). Effectiveness of spectroscopy in identification of swelling indicator clay minerals. *International Journal of Remote Sensing*, 25, 455–469.
- Kruse, F.A. (1988). Use of airborne imaging spectrometer data to map minerals associated with hydrothermally altered rocks in the northern grapevine mountains, Nevada, and California. *Remote Sensing of Environment*, 24, 31–51.
- Lagacherie, P., Baret, F., Feret, J. -B., Madeira Netto, J., & Robbez-Masson, J.M. (2008). Estimation of soil clay and calcium carbonate using laboratory, field and airborne hyperspectral measurements. *Remote Sensing of Environment*, 112, 825–835.
- Milliken, R.E., & Mustard, J.F. (2005). Quantifying absolute water content of minerals using near-infrared reflectance spectroscopy. *Journal of Geophysical Research, Planets*, 110, E12001.
- Murphy, R., Schneider, S., & Monteiro, S. (2014). Mapping layers of clay in a vertical geological surface using hyperspectral imagery: Variability in parameters of SWIR absorption features under different conditions of illumination. *Remote Sensing*, 6, 9104–9129.
- Mustard, J.F., Murchie, S.L., Pelkey, S.M., Ehlmann, B.L., Milliken, R.E., Grant, J.A., et al. (2008). Hydrated silicate minerals on Mars observed by the Mars Reconnaissance Orbiter CRISM instrument. *Nature*, 454, 305–309.
- Pelkey, S.M., Mustard, J.F., Murchie, S., Clancy, R.T., Wolff, M., Smith, M., et al. (2007). CRISM multispectral summary products: Parameterizing mineral diversity on Mars from reflectance. *Journal of Geophysical Research, Planets*, 112, E08S14.
- Roberts, D.A., Yamaguchi, Y., & Lyon, R.J.P. (1986). Comparison of various techniques for calibration of AIS data. *2nd AIS Workshop* (pp. 21–30). Pasadena, CA: Jet Propulsion Laboratory.
- Smith, G.M., & Milton, E.J. (1999). The use of the empirical line method to calibrate remotely sensed data to reflectance. *International Journal of Remote Sensing*, 20, 2653–2662.
- Vermote, E., Tanré, D., Deuzé, J., Herman, M., & Morcette, J. (1997). Second simulation of the satellite signal in the solar spectrum, 6S: An overview. *IEEE Transactions on Geoscience and Remote Sensing*, 35, 675–686.
- Viscarra Rossel, R.A., & Chen, C. (2011). Digitally mapping the information content of visible–near infrared spectra of surficial Australian soils. *Remote Sensing of Environment*, 115, 1443–1455.